Morphology and chemical state of Co-Mo catalysts for growth of single-walled carbon nanotubes vertically aligned on quartz substrates

Minghui Hu,[a] Yoichi Murakami,[b] Masaru Ogura,[a] Shigeo Maruyama,[b] Tatsuya Okubo [a,c,*]

[a] *Department of Chemical System Engineering, The University of Tokyo, 7-3-1 Hongo, Bunkyo-ku, Tokyo 113-8656, Japan*

[b] *Department of Mechanical Engineering, The University of Tokyo, 7-3-1 Hongo, Bunkyo-ku, Tokyo 113-8656, Japan*

[c] *PRESTO, JST, 7-3-1 Hongo, Bunkyo-ku, Tokyo 113-8656, Japan*

[*] Corresponding Author. Tel.: +81-3-58417348; fax: +81-3-58003806.

E-mail address: okubo@chemsys.t.u-tokyo.ac.jp (T. Okubo)

ABSTRACT

Bimetallic catalysts (Co:Mo ≈ 2:1 in atomic ratio) were prepared on quartz substrates from metal acetate solutions using a procedure of dip coating, followed by calcination and reduction. High-purity single-walled carbon nanotubes (SWNTs) 1–2 nm in diameter were grown densely (~1.0×10^{17} m^{-2}) and vertically on these substrates during an alcohol catalytic chemical vapor deposition process. To clarify the mechanism of the high selectivity and activity of these catalysts, we studied the morphology and chemical state of the Co-Mo catalysts during their preparation using transmission electron microscopy and X-ray photoelectron spectroscopy. The results showed that the stable existence of well-dispersed (~1.3×10^{17} m^{-2}) nano-sized (1–2 nm) catalyst particles composed of Co molybdates and metallic Co plays an important role in the SWNT growth. Based on these results, we propose a model to understand the good dispersion and high stability of these nano-sized catalyst particles against agglomeration during calcination and reduction.

Keywords: Co; Mo; Molybdate; Quartz; Single-walled carbon nanotubes; Catalytic chemical vapor deposition; Raman; XPS; TEM

1. Introduction

Single-walled carbon nanotubes [1] (SWNTs) exhibit superior chemical reactivity, electrical conductivity, optical activity, and mechanical property [2]. In contrast to arc discharge [3] and laser ablation [4] methods, catalytic chemical vapor deposition (CCVD) can produce large-scale SWNTs at low cost [5, 6]. Bimetallic Co-Mo catalysts, which have been studied for decades due to their high activity in hydrodesulfurization [7, 8], attract much attention owing to their high selectivity [9-12] for the SWNT growth. Especially, Co-Mo catalysts prepared from metal acetate solutions followed by an alcohol CCVD process [13] can directly produce high-purity SWNTs randomly [14] or vertically aligned [15] on quartz glass substrates without supporting materials. These achievements will definitely promote the innovation of glass- and silicon-based SWNT device systems.

The mechanism of high selectivity and activity for Co-Mo catalysts in controlling the growth and structure of SWNTs has not been fully clarified yet. For catalysts with different compositions, their catalytic performances in the SWNT growth have the following order: Co-Mo acetates > Co (nitrates)-Mo (acetates) >> Co acetates >> Mo acetates [16]. Although it is suggested that at an optimum Co/Mo ratio, Co molybdate upperlayers or underlayers stabilize Co species during reduction, and Mo carbides release active carbon to catalytic metallic Co particles from which SWNTs selectively grow during the CVD reaction [17-20], the correlation between the morphology and the chemical state of Co-Mo catalysts during their preparation and activation has never been

verified. The effect of Mo in bimetallic catalysts on the growth of SWNTS still remains to be clarified.

In this study, to resolve these questions, we prepared Co-Mo catalysts on quartz substrates from metal acetate solutions using a procedure of dip coating, followed by calcination and reduction, instead of using single crystals or porous materials as catalyst support. This permits us to quantitatively characterize the catalyst morphology at the nanoscale using transmission electron microscopy (TEM), and the chemical state of metal species using X-ray photoelectron spectroscopy (XPS). Based on critical evidence discovered in our experiment, a model is then developed to understand why Co-Mo catalysts prepared with the above method show high selectivity and activity for the growth of high-purity SWNTs densely and vertically aligned on quartz substrates during the alcohol CCVD process.

2. Experimental

2.1 Catalyst preparation and SWNT growth

Co-Mo catalysts were prepared on fused quartz glass substrates using a procedure of dip coating, followed by calcination and reduction [14]. Firstly, as-delivered quartz substrates ($25\times25\times0.5$ mm^3) were baked in air at 500 °C for 5 min in an electric furnace just before the supporting process. Then, Co acetate $(CH_3COOH)_2Co\text{-}4H_2O$ and Mo acetate $(CH_3COOH)_2Mo$ (Co:Mo = 0.01:0.01 % wt which was defined as the atomic weight of metallic Co and Mo to the weight of solutions, and Co:Mo = 1.6:1 in atomic ratio) in ethanol solutions were dip-coated onto these substrates at a withdrawal speed

of 4 cm min^{-1}. After drying in air at room temperature (r.t.), the substrates were calcined in an open furnace at 400 °C for 5 min. These substrates are referred to as calcined catalysts/substrates hereafter.

Then, the activation of these calcined Co-Mo catalysts was performed with a reduction process prior to the CVD reaction. These freshly calcined substrates were immediately transferred from the furnace into a tubular CVD reactor that was then evacuated to < 2×10^{-2} Torr by a rotatory pomp. They were heated from r.t. to 800 °C in 30 min in an Ar/H_2 (3% H_2) stream of 300 sccm at 300 Torr. These substrates are referred to as reduced catalysts/substrates hereafter.

Finally, the growth of SWNTs was performed with an alcohol CCVD process [15]. Immediately after reduction, ethanol vapor was supplied as a carbon source (10 Torr) mixed with an Ar/H_2 (3% H_2) stream (300 sccm, 7 Torr) at 800 °C. After reaction for 1 h, the substrates were cooled to r.t. in an Ar/H_2 stream. These products are referred to as as-grown SWNTs hereafter.

2.2 Characterization of SWNTs and catalysts

The quality and structure of the as-grown SWNTs were investigated using micro-Raman scattering and scanning electron microscopy (SEM). Raman scattering measurements were done using a Chromex 501is spectrometer and an Andor DV401-FI CCD system equipped with a Seki Technotron STR250 optical system. SEM observations were done using a Hitachi S-900 and S-5200.

The morphology of Co-Mo catalysts after calcination and after reduction was characterized using TEM. The samples for plan-view TEM observations were

sputter-coated with a 10-nm SiO_2 layer to avoid structural variation during TEM observations. For the samples for XTEM observations, two identical substrates were adhered to each other from the catalyst side by using glue without depositing a SiO_2 layer. The samples for plan-view TEM and XTEM observations had a sandwich structure of SiO_2(quartz)/catalyst/SiO_2(10nm) and SiO_2(quartz)/catalyst/glue/catalyst/SiO_2(quartz), respectively. Then, these substrates were sliced and punched into circular discs with a diameter of 3 mm and a thickness of 2 mm. Finally, these discs were further thinned by conventional mechanical grinding, polishing, and dimpling, followed by Ar ion milling at an acceleration voltage 4 kV at an incidence angle of 6° with a Gatan 691 Precision Ion Polishing System (PIPS). Plan-view TEM and XTEM observations were done using a JEOL JEM-4000EX at 400 kV and 2010F at 200 kV, respectively. Because there is no crystalline orientation information from the fused quartz substrates, no orientation adjustment during XTEM observations was performed to make the incident angle of electron beam parallel to the direction of quartz-glue interfaces.

The chemical state of Co-Mo catalysts after calcination and after reduction was characterized using XPS. The measurements were done using a PHI 1600 X-ray photoelectron spectrometer equipped with an Mg Kα (1253.6 eV) source operating at 300 W. To decrease the influence of oxidation and contamination for XPS samples, these substrates were sealed in a plastic box filled with Ar gas as soon as they were removed from the furnace or the CVD reactor, and then transferred to an analysis chamber (2.0×10^{-9} Torr) through a loading chamber (5.3×10^{-6} Torr) for XPS measurements. All these procedures were finished in 30 min. Binding energies (BEs) were referenced to the C 1s peak at 284.6 eV to compensate for the charging effect. The

BE curves were fitted using a mixed Gaussian/Lorentzian curve after subtracting the background using the Shirley algorithm [21], in which spin-orbital-splitting intensities were fixed at their theoretical ratios. The surface atomic ratios of the calcined and the reduced quartz substrates coated with Co-Mo catalysts were estimated from peak intensities in the XPS spectra and atomic sensitivity factors.

3. Results

3.1 Structure and morphology of as-grown SWNTs

Figure 1 shows the Raman spectra of the as-grown SWNTs on the quartz substrates measured with 488-nm excitation. The strong peak at 1590 cm^{-1} (G-band) arises from an in-plane oscillation of carbon atoms in the sp^2 graphene sheet. The weak peak at 1340 cm^{-1} (D-band) reflects the degree of defects or dangling bonds contained in the sp^2 arrangement of graphene sheet. The G/D ratio as high as 20–30 indicates the highly selective growth of high-purity SWNTs. Moreover, the absence of multi-walled carbon nanotubes (MWNTs) and amorphous impurities has been confirmed by previous TEM observations [15]. As indicated by the Raman spectrum of "radial breathing mode" (RBM) of these as-grown SWNTs, these SWNTs had diameters of 1–2 nm, which was estimated according to the relationship $d = 248 / \upsilon$, where d (nm) is the diameter and υ (cm^{-1}) is the Raman shift of a SWNT [22, 23].

Figure 2 shows the morphology of the as-grown SWNTs on the quartz substrates at a titled angle. The SWNTs self-assembled into bundles ~1.5 μm in length, and these bundles were densely and vertically aligned on the substrates. The number density of

these SWNTs was estimated to be ~1.0×10^{17} m^{-2} from the density of bundles and the number of SWNTs per bundle [15].

3.2 Morphology of calcined and reduced Co-Mo catalysts

First, it is noteworthy that the reduced samples for TEM observations should be considerably oxidized even if the catalysts are in metallic state right after reduction due to the following two reasons: 1) An oxide layer or a glue layer was coated on the catalysts; 2) More than two weeks was taken to prepare the TEM samples ready for observation.

Figure 3 shows plan-view TEM images of the calcined and the reduced Co-Mo catalysts on the quartz substrates. For both samples, as shown in Figs. 3(a) and 3(d), well-dispersed nano-sized particles with diameters of 1–2 nm can be observed. Figures 3(b) and 3(e) show that the Co-Mo catalyst particles after reduction seemed to shrink to a smaller size, while remaining good dispersion without agglomerating into larger ones. The number density of these uniformly distributed catalyst particles after reduction was estimated from the TEM images to be as high as ~1.3×10^{17} m^{-2}.

Selected area electron diffraction (SAED) patterns shown in the insets of Figs. 3(a) and 3(d), and high-resolution TEM (HRTEM) images shown in Figs. 3(b) and 3(e) revealed that most of the nano-sized catalyst particles were amorphous, and only some of them were crystalline. As indicated in Figs. 3(c) and 3(f), these crystalline particles exhibit lattice distances of 2.13–2.38 Å, which are approximately consistent with CoO (200) lattice constant (2.13 Å), but significantly differ from those of Co (111) (2.05 Å), Co_3O_4 (311) (2.44 Å), MoO_2 (110, $1\bar{1}$) (3.41 Å), MoO_3 (021) (3.26 Å), and $CoMoO_4$

(002, 220) (3.36 Å) lattices. Because Co:Mo = 1.6:1 in ethanol solutions, the amount of Co species should be in excess on the substrates. Therefore, we conclude that most of those nano-sized particles, whether crystalline or amorphous, might be mainly composed of CoO. This conclusion is supported with the surface composition analysis using XPS, which is shown in the next section.

Figure 4 shows XTEM images of the reduced Co-Mo catalysts on the quartz substrates. Because the incident angle of electron beam deviated from the parallel direction of quartz-glue interfaces, as shown in Fig. 4(a), catalyst particles were seemingly located within a vertical range of ~ 10 nm. High-resolution XTEM images in Fig. 4(b) exhibited that these spherical- or elliptical-like particles with diameters of 1–2 nm were well dispersed without aggregation, which is consistent with corresponding plan-view images.

The above results indicate that Co-Mo catalysts existed as well-dispersed nano-sized particles on the quartz substrates just before the CVD reaction. This morphology should be closely associated with the subsequent growth of densely and vertically aligned SWNTs. Further analyses of chemical state of Co-Mo catalysts using XPS provide us a more clear comprehension of the mechanism why these nano-sized catalyst particles with such a high number density can be formed and stably exist without agglomeration during calcination and reduction.

3.3 Chemical state of calcined and reduced Co-Mo catalysts

Figure 5 shows BEs of C 1s, Si 2p, and O 1s levels for the calcined and the reduced catalysts on the quartz substrates. As indicated in Figs. 5(b) and 5(c), the BEs of Si 2p at

103.4–103.6 eV, and O 1s at 532.3–532.5 eV agree well with quartz references (Si: 103.3–103.7 eV, O: 532.1–532.7 eV) [24, 25]. This suggests that the BE shift due to the charging effect has been corrected well with the C 1s BE as a reference. The spectra of C 1s and Si 2p indicate the absence of acetate residues (288.2–289.3 eV) [26, 27], metal carbides (282.7–283.1 eV) [28, 29], and metal silicides (99.1–99.6 eV) [30-32]. Moreover, the spectra of O 1s indicate the formation of metal oxide species (530.3–530.4 eV) [33].

Figure 6 shows BEs of Mo 3d levels for the calcined and the reduced catalysts on the quartz substrates. Both spectra exhibit a pair of spin-orbit BEs at 232.4–232.5 and 235.4–235.5 eV, whereas a pair of new spin-orbit BEs appeared at 229.0 and 232.0 eV only for the reduced catalysts. The Mo $3d_{5/2}$ BE at 232.4–232.5 eV is attributed to Mo^{6+} in MoO_3 (232.2–233.0 eV) [17, 34-38] and/or non-stoichiometric Co molybdates, $CoMoO_x$ (232.1–232.3 eV for stoichiometric Co molybdates where x = 4) [17, 37, 38]. The new Mo $3d_{5/2}$ BE at 229.1 eV is attributed to Mo^{4+} in MoO_2 (229.0–230.1 eV) [17, 34-37]. These results indicate that the decomposition of Mo acetates resulted in the formation of Mo^{6+} in MoO_3 and/or $CoMoO_x$, and the reduction of calcined catalysts converted Mo oxide species to MoO_y ($y \leq 2$) or even metallic Mo that was not detected due to its oxidization during ex-situ XPS analyses.

Figure 7 shows BEs of Co 2p levels for the calcined and the reduced Co-Mo catalysts on the quartz substrates. The reduced samples showed remarkable differences from calcined ones in two aspects. One is the appearance of a new BE at 777.8 eV, which is attributed to metallic Co (777.8–778.5 eV) [17, 37, 39, 40]. The other is the decreased distance between the $2p_{3/2}$ and $2p_{1/2}$ spin-orbit BEs by as large as 1.6 eV, while the $2p_{1/2}$ BE remained almost unchanged. This should result from the change in chemical state of

Co oxide species during reduction, rather than from the charging effect due to particle sizes [41] or layered structures [42] with different dielectric properties.

To clarify the above changes, we decomposed and fitted the Co $2p_{3/2}$ BEs, as shown in Fig. 8. The spectra for calcined and the reduced catalysts are composed of two $2p_{3/2}$ components at 780.9–781.0 eV and 783.3–783.5 eV, and two distinct shake-up satellites at 786.9–787.0 eV and 790.2–790.6 eV. The two $2p_{3/2}$ BEs are attributed to Co^{2+} oxide species based on these intense shake-up satellites 6.0–6.5 eV higher than the primary spin-orbit BEs [38, 43]. The two $2p_{3/2}$ BEs at 780.9–781.0 eV and 783.3–783.5 eV are further assigned to Co^{2+} in CoO and Co^{2+} in $CoMoO_x$, respectively, due to their agreement with CoO (780.0–780.7 eV) [17, 39, 40, 44, 45] and $CoMoO_4$ (780.5–781.2) [37-39, 46] references. The relatively large BE deviation of Co^{2+} in $CoMoO_x$ from Co^{2+} in $CoMoO_4$ might result from the polarization effect or the non-stoichiometry when Co^{2+} ions are incorporated into highly oxidized MoO_3 matrix [39, 46, 47]. The BE intensity ratio of Co^{2+} in $CoMoO_x$ to that in CoO increased from 1.3 to 2.6 after reduction, indicating that more $CoMoO_x$ was formed at the expense of CoO and MoO_3. This change leads to the seemingly decreased distance between Co $2p_{3/2}$ and $2p_{1/2}$ BEs shown in Fig. 7. Therefore, we conclude that the calcination of dip-coated substrates decomposed Co acetates into Co oxide species existing as CoO and $CoMoO_x$, and the subsequent reduction resulted in the formation of metallic Co and more $CoMoO_x$.

Table 1 shows the surface atomic ratios of the calcined and the reduced quartz substrates coated with Co-Mo catalysts. The quantity of metals as low as less than 10% of the total composition supports the approximate estimation in the experimental section that the quartz substrates might be covered with the metallic catalyst layers. The calcined and the reduced samples had Co/Mo atomic ratios of 2.1–2.3, approximately

consistent with the initial ratio of 1.6 in metal acetate solutions, so that only excess Co species were observed in TEM images. It is noteworthy that the atomic ratios of Co and Mo to total elements decreased by 63% and 68% after reduction, respectively, which could be explained from the decrease in catalyst coverage, i.e., the decrease in catalyst particle size, as confirmed in TEM images.

4. Discussion

Based on the above results, we propose a model, as illustrated in Fig. 9, to describe the evolution in morphology and chemical state of Co-Mo catalysts on the quartz substrates during calcination and reduction. We assume that a layer of bimetallic catalysts (Co:Mo ≈ 2:1 in atomic ratio) is formed on the quartz substrates after the dip coating from dilute metal acetate solutions. After calcination in air at 400 °C, metal acetates are decomposed into CoO, $CoMoO_x$ (x = 4 for stoichiometric Co molybdates), and MoO_3, which exist as well-dispersed nano-sized particles. After reduction in Ar/H_2 up to 800 °C, existing $CoMoO_x$ remains unchanged, whereas CoO and MoO_3 are reduced into Co and MoO_y ($y \leq 2$), and more $CoMoO_x$ are formed at the expense of Co and MoO_3. During this process, no distinct agglomeration occurs although catalyst particles partially de-wet into smaller sized ones, as discussed later. Finally, the growth of SWNTs starts with the reaction of the ethanol vapor and metallic Co particles.

We deduce that when Mo and Co species uniformly coexist on SiO_2 surfaces during calcination, Mo preferentially promotes the formation of metal oxides at catalyst/SiO_2 interfaces, because Mo has a stronger affinity to oxygen than Co [48]. Because Co:Mo ≈ 2:1 in atomic ratio, the excess Co easily diffuses into MoO_3 [46], and forms $CoMoO_x$

underlayers/boundaries, whereas the residue Co exists as CoO particles either located on $CoMoO_x$ underlayers or attached to $CoMoO_x$ boundaries.

The formation of well-dispersed nano-sized catalyst particles during calcination is attributed mainly to the decomposition of metal acetates on oxide substrates. It is suggested that the strong coordination of carboxylic groups with metal ions mediates the decomposition of metal acetates to prevent the formation of large particles [49, 50]. As a result, compared with metal nitrates, metal acetates form better dispersed nano-sized particles during calcination [49, 50], thereby accounting for their best performance for the growth of SWNTs [16].

As the temperature rises from r.t. during reduction, CoO and MoO_3 in Ar/H_2 start to be reduced into metallic Co and MoO_y, respectively, whereas $CoMoO_x$ remains unchanged due to their extreme stability against reduction [51, 52]. These metallic Co was detected in XPS analyses under particular protection from exposure to oxygen, whereas only metal oxides were confirmed in TEM observations. In addition, the decreased CoO intensity and the increased $CoMoO_x$ intensity support the following deduction. The firstly reduced metallic Co reacts with MoO_3/MoO_y until Mo oxides are depleted, and the residue Co remains metallic. That is, the formation of metallic Co possibly competes with that of Co molybdates, and finally becomes dominant.

The stable existence of well-dispersed nano-sized Co particles during reduction is attributed to the immobilization effect of $CoMoO_x$ underlayers. Although metallic Co particles vigorously migrate on SiO_2 surfaces [40], they should be easily trapped on $CoMoO_x$ underlayers, owing to the strong interactions between MoO_3 and metallic Co [46]. The decreased size and the spherical- or elliptical-like shape of catalyst particles after reduction, which were observed in plan-view TEM and XTEM images, suggest

that metallic Co might de-wet on quartz substrates. This deduction was confirmed by the decreased metal/substrate atomic ratio after reduction indicated by XPS analyses [40]. Although these metallic Co particles de-wet partially on $CoMoO_x$, their interfacial interactions are strong enough to limit their mobility and prevent them from agglomerating into large particles. Therefore, we conclude that the role of Mo in bimetallic Co-Mo catalysts is to stabilize well-dispersed nano-sized metallic Co particles from agglomeration. Without Mo [16, 40] or $CoMoO_x$ [19, 38], the catalyst selectivity for the growth of SWNTs decreases or even disappears due to the agglomeration of Co particles.

Generally, the growth of SWNTs requires catalyst particles with diameters less than 2–3 nm [53-56]. These well-dispersed Co particles with diameters of 1–2 nm and a number density of $\sim 1.3\times10^{17}$ m^{-2} directly confirmed in HRTEM images correlate well with the selective growth of high-purity vertically aligned SWNTs with diameters of 1–2 nm and a number density of $\sim 1.0\times10^{17}$ m^{-2}. This proves convincingly the extremely high catalytic activity and efficiency of these nano-sized particles.

During the alcohol CVD reaction, because Mo is catalytically inactive at ~800 °C [16], the SWNTs might only grow from metallic Co particles. These SWNTs interact with neighboring nanotubes via van der Waals forces to self-assemble into rigid bundles. These bundles are so populated that they have to grow only upright from the substrate surfaces due to the space restriction, similar to the case of vertically aligned MWNTs [57, 58]. As the SWNTs lengthen, their growth should be limited by the diffusion of ethanol vapor through the narrow space between nanotubes/bundles. The continuous supply of H_2 together with ethanol vapor during the CVD reaction might enable Co particles to remain highly active throughout the nucleation and growth of SWNTs.

Without feeding H_2 during the alcohol CCVD process, the SWNTs only grow sparsely in a random orientation [14].

Besides Co-Mo systems, other X-Y bimetallic systems (X = Fe, Co, and Ni; Y = Ti, Cr, Mo, W, and Al) [59-67], should act as excellent catalysts to the SWNT growth or other reactions due to similar mechanism. Here, X is a VIII-group element known as monometallic catalysts for the SWNT growth, and Y is mainly an IVB-, VB-, and VIB-group element capable of forming stable high-valent oxides due to their vacant *d* orbital. It is believed that the formation of XY_mO_n-like (m = 1–2, n = 3–4) oxide complex stabilizes the highly-dispersed nano-sized particles, which show high catalytic performances.

This study revealed that the stable existence of well-dispersed nano-sized catalytic metal particles is indispensable for the growth of SWNTs densely and vertically aligned on the quartz substrates. In addition to that, the CCVD process with ethanol as a carbon source also plays an important role in the selective growth of high-purity SWNTs. An appropriate amount of oxygen radicals generated from the decomposition of ethanol on catalytic metal particles removes amorphous carbon impurities with dangling bonds in the growing SWNTs [68]. The combination of the Co-Mo catalysts prepared from metal acetate solutions and the alcohol CCVD process satisfies the requirement of (1) strict control of chemical state and morphology of catalyst particle and (2) in-situ purification of produced SWNTs, thereby being able to fabricate vertically aligned SWNTs with high selectivity and high purity. However, some issues on the working state of these catalysts during the CVD reaction, such as the chemical state and its contribution to the growth of SWNTs, need further investigation.

5. Conclusions

High-purity SWNTs with diameters of 1–2 nm were grown densely (~1.0×10^{17} m^{-2}) and vertically on the quartz substrates where bimetallic Co-Mo catalysts with a stoichiometry of ~2 were dip-coated from metal acetate solutions, followed by calcination and reduction. HRTEM and XPS studies on the morphology and chemical state of the calcined and the reduced catalysts provided critical evidence for their catalytic mechanism.

The results show that calcination in air at 400 °C decomposes metal acetates into metal oxide species composed of CoO, MoO_3 and $CoMoO_x$ (x = 4 for stoichiometric Co molybdates), which exist as well-dispersed nano-sized particles possibly due to the mediation of strong coordination of carboxylic groups with metal ions during the acetate decomposition. The excess CoO might be either located on or attached to $CoMoO_x$ underlayers/boundaries. After reduction in Ar/H_2 up to 800 °C, metallic Co, MoO_y ($y \leq 2$) and more $CoMoO_x$ are formed at the expense of CoO and MoO_3. The strong interactions between metallic Co and $CoMoO_x$ underlayers prevent these well-dispersed (~1.3×10^{17} m^{-2}) nano-sized (1–2 nm) catalyst particles against agglomerating into larger ones.

The good dispersion of nano-sized catalyst particles due to the acetate decomposition, their stability against agglomeration due to the interactions between Co and $CoMoO_x$, their high activity due to the continuous supply of H_2 throughout the CVD reaction, and the in-situ purification of growing SWNTs due to the oxygen radicals generated from the ethanol decomposition lead to the highly selective growth of high-purity SWNTs densely and vertically aligned on the quartz substrates.

Acknowledgments

We gratefully acknowledge Prof. Y. Shimogaki (The University of Tokyo) for his support in the XPS analyses, Mr. H. Tsunakawa (The University of Tokyo) for his assistance in TEM observations, and Mr. T. Sugawara (The University of Tokyo) for his technical advice about SEM observations. Part of this work was financially supported by 13555050 from JSPS and #13GS0019 from MEXT.

Figure legends

Figure 1. Raman spectra of as-grown SWNTs on quartz substrates measured with 488-nm excitation.

Figure 2. Cross-sectional SEM image of as-grown SWNTs on quartz substrates, observed at a fracture edge at a tilted angle.

Figure 3. Plan-view TEM images of (a) calcined and (d) reduced Co-Mo catalysts on quartz substrates, and HRTEM images of (b) (c) calcined and (e) (f) reduced Co-Mo catalysts. SAED patterns are shown in the insets of (a) and (d).

Figure 4. (a) XTEM and (b) HRXTEM images of reduced Co-Mo catalysts on quartz substrates.

Figure 5. XPS spectra of (a) C 1s, (b) Si 2p, and (c) O 1s levels for calcined and reduced Co-Mo catalysts on quartz substrates.

Figure 6. XPS spectra of Mo $3d_{5/2}$ and $3d_{3/2}$ levels for calcined and reduced Co-Mo catalysts on quartz substrates.

Figure 7. XPS spectra of Co $2p_{3/2}$ and $2p_{1/2}$ levels for calcined and reduced Co-Mo catalysts on quartz substrates.

Figure 8. XPS spectra of Co $2p_{3/2}$ levels for calcined and reduced Co-Mo catalysts on quartz substrates.

Figure 9. Chemical state and morphology of Co-Mo catalysts on quartz substrates after (a) calcination and (b) reduction.

Table 1. Surface composition of quartz substrates dip-coated with Co-Mo catalysts after calcination and after reduction.

Samples	Atomic ratio (%)				
	Co	Mo	Si	O	C
Calcined	5.1	2.2	27.9	59.7	5.1
Reduced	3.2	1.5	29.8	61.7	3.7

References

[1] S. Iijima, T. Ichihashi, Nature 363 (1993) 603.

[2] R. Saito, G. Dresselhaus, M.S. Dresselhaus (Ed.), Physical Properties of Carbon Nanotubes, 1st ed., Imperial College Press, London, 1998.

[3] C. Journet, W.K. Maser, P. Bernler, A. Loiseau, M.L. de la Chapelle, S. Lefrant, P. Denlard, R. Lee, J.E. Fischer, Nature 388 (1997) 756.

[4] A. Thess, R. Lee, P. Nikolaev, H.J. Dai, P. Petit, Robert. J, C.H. Xu, Y.H. Lee, S.G. Kim, A.G. Rinzler, D.T. Colbert, G.E. Scuseria, D. Tomanek, J.E. Fischer, R.E. Smalley, Science 273 (1996) 483.

[5] J. Kong, A.M. Cassell, H.J. Dai, Chem. Phys. Lett. 292 (1998) 567.

[6] M. Su, B. Zheng, J. Liu, Chem. Phys. Lett. 322 (2000) 321.

[7] H. Topsoe, B.S. Clausen, R. Candia, C. Wivel, S. Morup, J. Catal. 68 (1981) 433.

[8] Y. Okamoto, T. Kubota, Catal. Today 86 (2003) 31.

[9] B. Kitiyanan, W.E. Alvarez, J.H. Harwell, D.E. Resasco, Chem. Phys. Lett. 317 (2000) 497.

[10] H. Ago, S. Ohshima, K. Uchida, M. Yumura, J. Phys. Chem. B 105 (2001) 10453.

[11] Y.J. Yoon, J.C. Bae, H.K. Baik, S.J. Cho, S. Lee, K.M. Song, N.S. Myung, Physica B 323 (2002) 318.

[12] W.E. Alvarez, F. Pompeo, J.E. Herrera, L. Balzano, D.E. Resasco, Chem. Mater. 14 (2002) 1853.

[13] S. Maruyama, R. Kojima, Y. Miyauchi, S. Chiashi, M. Kohno, Chem. Phys. Lett. 360 (2002) 229.

[14] Y. Murakami, Y. Miyauchi, S. Chiashi, S. Maruyama, Chem. Phys. Lett. 377 (2003) 79.

[15] Y. Murakami, S. Chiashi, Y. Miyauchi, M. Hu, M. Ogura, T. Okubo, S. Maruyama, Chem. Phys. Lett. 385 (2004) 298.

[16] Y. Murakami, S. Chiashi, Y. Miyauchi, S. Maruyama, Jpn. J. Appl. Phys. 43 (2004) 1221.

[17] J.E. Herrera, L. Balzano, A. Borgna, W.E. Alvarez, D.E. Resasco, J. Catal. 204 (2001) 129.

[18] W.E. Alvarez, B. Kitiyanan, A. Borgna, D.E. Resasco, Carbon 39 (2001) 547.

[19] J.E. Herrera, D.E. Resasco, J. Catal. 221 (2003) 354.

[20] J.E. Herrera, D.E. Resasco, J. Catal. 221 (2004) 354.

[21] D.A. Shirley, Phys. Rev. B 135 (1972) 4709.

[22] R. Saito, G. Dresselhaus, M.S. Dresselhaus, Phys. Rev. B 61 (2000) 2981.

[23] A. Jorio, R. Saito, J.H. Hafner, C.M. Lieber, M. Hunter, T. McClure, G. Dresselhaus, M.S. Dresselhaus, Phys. Rev. Lett. 86 (2001) 1118.

[24] C.D. Wagner, D.E. Passoja, H.F. Kinisky, H.A. Six, W.T. Jansen, J.A. Taylor, J. Vac. Sci. Technol. 21 (1982) 933.

[25] Y. Duval, J.A. Mielczarski, O.S. Pokrovsky, E. Mielczarski, J.J. Ehrhardt, J. Phys. Chem. B 106 (2002) 2937.

[26] U. Gelius, P.F. Heden, J. Hedman, B.J. Lindberg, R. Manne, R. Nordberg, C. Nording, K. Siegbahn, Phys. Scr. 2 (1970) 70.

[27] S.B.M. Hagstrom, P.O. Heden, H. Lofgren, Solid State Commun. 8 (1970) 1245.

[28] L. Ramqvist, K. Hamrin, G. Johannson, A. Fahlman, C.J. Nording, J. Phys. Chem. Solids 30 (1969) 1835.

[29] H. Wang, S.P. Wong, W.Y. Cheung, N. Ke, W.F. Lau, M.F. Chiah, X.X. Zhang, Mater. Sci. Eng. C 16 (2001) 147.

[30] W.A. Brainard, D.R. Wheeler, J. Vac. Sci. Technol. 15 (1978) 1801.

[31] J.S. Pan, E.S. Tok, C.H.A. Huan, R.S. Liu, J.W. Chai, W.J. Ong, K.C. Toh, Surf. Sci. 532-535 (2003) 639.

[32] I. Jarrige, P. Jonnard, P. Holliger, T.P. Nguyen, Appl. Surf. Sci. 212-213 (2003) 689.

[33] V.I. Nefedov, D. Gati, B.F. Dzhurinskii, N.P. Sergushin, Y.V. Salyn, Zh. Neorg. Khim. 20 (1975) 2307.

[34] B.R. Quincy, M. Houalla, A. Proctor, D.M. Hercules, J. Chem. Phys. (1990) 1520.

[35] F. Solymosi, J. Cserenyi, A. Szoke, T. Bansagi, A. Oszko, J. Catal. 165 (1997) 150.

[36] G. Chen, T.E. Ford, C.R. Clayton, J. Colloid Interface Sci. 204 (1998) 237.

[37] M. Probst, M. Vob, R. Denecke, L. Viscido, J.M. Heras, D. Borgmann, H.-P. Steinruck, J. Electron Spectrosc. Relat. Phenom. 114-116 (2001) 539.

[38] V.L. Parola, G. Deganello, C.R. Tewell, A.M. Venezia, Appl. Catal. A 235 (2002) 171.

[39] R. Kleyna, H. Mex, M. Vos, D. Borgmann, L. Viscido, J.M. Heras, Surf. Sci. 433-434 (1999) 723.

[40] R. Riva, H. Miessner, R. Vitali, G.D. Piero, Appl. Catal. A 196 (2000) 111.

[41] V.I. Bukhtiyarov, I.P. Prosvirin, R.I. Kvon, S.N. Goncharova, B.S. Balzhinimaev, J. Chem. Soc., Faraday Trans. 93 (1997) 2323.

[42] S. Suzer, Anal. Chem. 75 (2003) 7026.

[43] M. Hassel, H.-J. Freund, Surf. Sci. 325 (1995) 163.

[44] W.-J. Wang, Y.-W. Chen, Appl. Catal. A 77 (1991) 223.

[45] Y. Brik, M. Kacimi, M. Ziyad, F. Bozon-Verdurazy, J. Catal. 202 (2001) 118.

[46] L. Viscido, M. Vob, D. Borgmann, J.M. Heras, J. Mol. Catal. A 167 (2001) 199.

[47] V.A. Zazhigalov, J. Haber, J. Stoch, A. Pyatnitzkaya, G.A. Komashko, V.M. Belousov, Appl. Catal. A 96 (1993) 135.

[48] M. Hu, S. Noda, H. Komiyama, Surf. Sci. 513 (2002) 530.

[49] T. Matsuzaki, K. Takeuchi, T. Hanaoka, H. Arakawa, Y. Sugi, Catal. Today 28 (1996) 251.

[50] S. Sun, N. Tsubaki, K. Fujimoto, Appl. Catal. A 202 (2000) 121.

[51] M. Deboer, E.P.F.M. Koch, R.J. Blaauw, E.R. Stobbe, A.N.J.M. Hoffmann, L.A. Boot, A.J. Vandillen, J.W. Geus, Solid State Ionics 63-65 (1993) 736.

[52] A.A. Halawy, M.A. Mohamed, G.C. Bond, J. Chem. Technol. Biotechnol. 58 (1993) 237.

[53] H. Dai, A.G. Rinzler, P. Nikolaev, A. Thess, D.T. Colbert, R.E. Smalley, Chem. Phys. Lett. 260 (1996) 471.

[54] S.B. Sinnott, R. Andrews, D. Qian, A.M. Rao, Z. Mao, E.C. Dickey, D. F., Chem. Phys. Lett. 315 (1999) 25.

[55] C.L. Cheung, A. Kurtz, H. Park, C.M. Lieber, J. Phys. Chem. B 106 (2002) 2429.

[56] Y. Shibuta, S. Maruyama, Chem. Phys. Lett. 382 (2003) 381.

[57] Z.F. Ren, Z.P. Huang, J.W. Xu, J.H. Wang, P. Bush, M.P. Siegal, P.N. Provencio, Science 282 (1998) 1105.

[58] S. Fan, M.G. Chapline, N.R. Franklin, T.W. Tombler, A.M. Cassell, H. Dai, Science 283 (2002) 512.

[59] B. Benaichouba, P. Bussiere, J.C. Vedrine, Appl. Catal. A 130 (1995) 31.

[60] J. Jankowski, G. Thomas, L.P. Camby, Solid State Ionics 101-103 (1997) 1321.

[61] L. An, J.M. Owens, L.E. McNeil, J. Liu, J. Am. Chem. Soc. 124 (2002) 13688.

[62] M. Vob, D. Borgmann, G. Wedler, J. Catal. 212 (2002) 10.

[63] B. Chen, G. Parker II, J. Han, M. Meyyappan, A.M. Cassell, Chem. Mater. 14 (2002) 1891.

[64] A. Valentini, N.L.V. Carreno, L.F.D. Probst, P.N. Lisboa-Filho, W.H. Schreiner, E.R. Leite, E. Longob, Appl. Catal. A 255 (2003) 211.

[65] T. Xiao, T. Suhartanto, A.P.E. York, J. Sloan, M.L.H. Green, Appl. Catal. A 253 (2003) 225.

[66] G.A. El-shobaky, A.M. Ghozza, G.M. Mohamed, Appl. Catal. A 241 (2003) 235.

[67] J.E. Herrera, D.E. Resasco, J. Phys. Chem. B 107 (2003) 3738.

[68] S. Maruyama, Y. Murakami, Y. Shibuta, Y. Miyauchi, S. Chiashi, J. Nanosci. Nanotech. 4 (2004) 1.

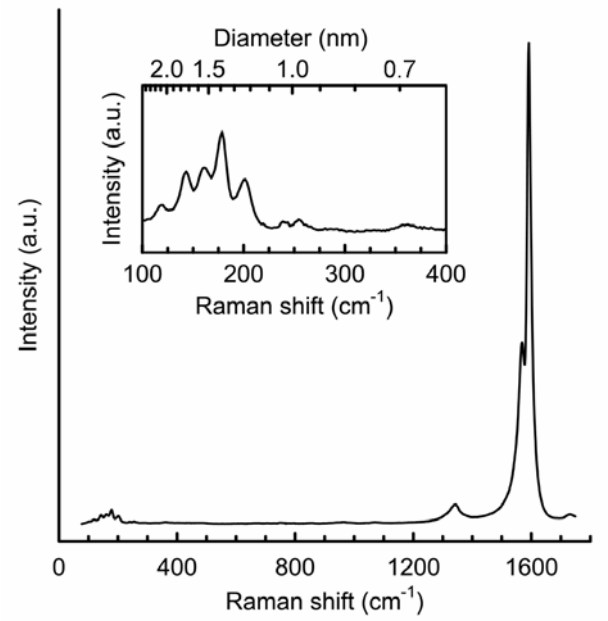
Diameter (nm)
2.0 1.5
1.0
0.7
Intensity (a.u.)
100
200
300
400
Raman shift (cm-1)
Intensity (a.u.)
0
400
800
1200
1600
Raman shift (cm-1)

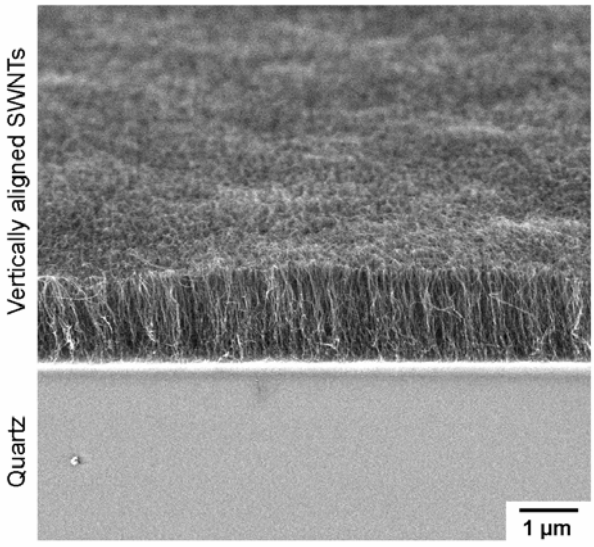
Vertically aligned SWNTs
Quartz
1 µm

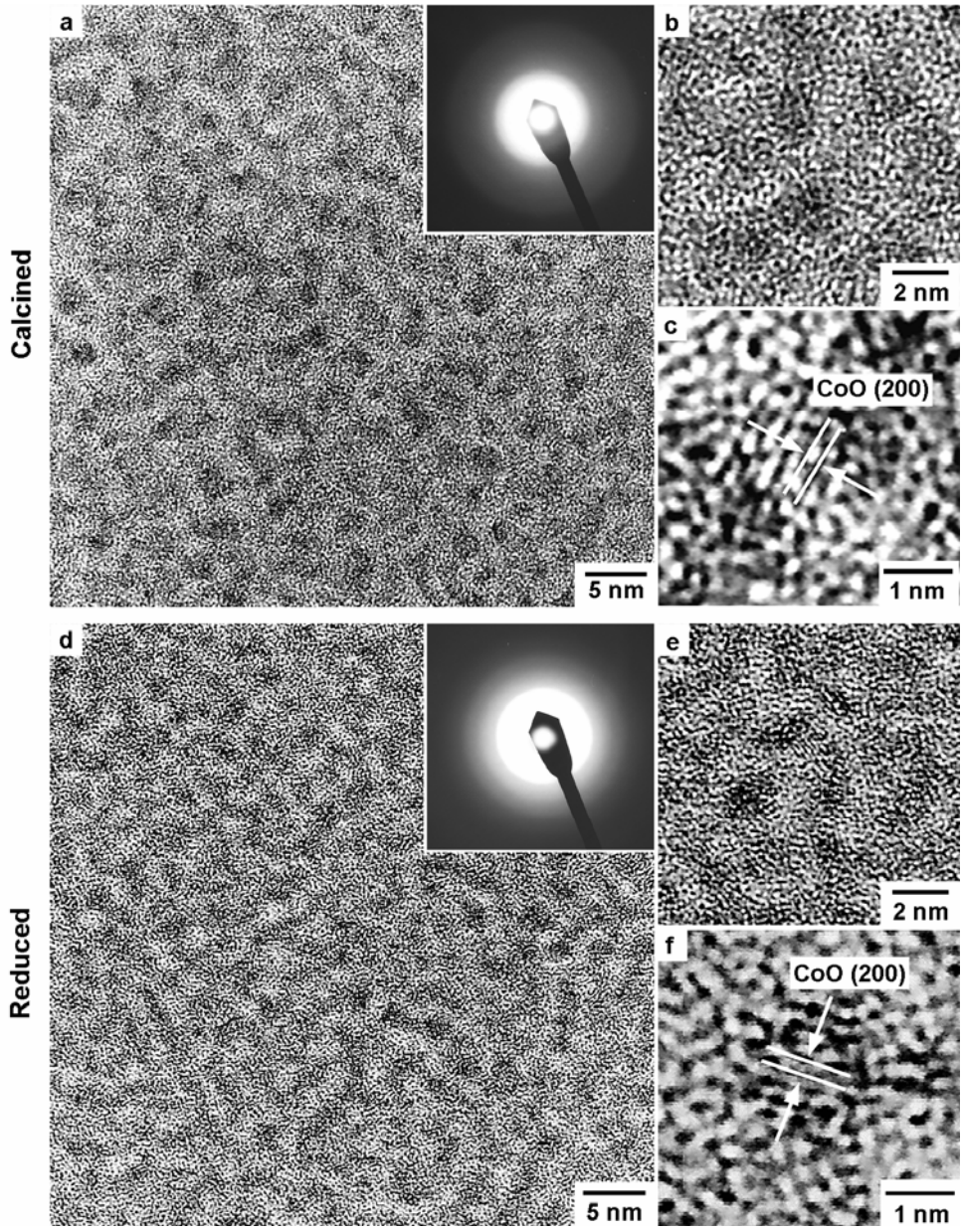
Calcined
Reduced
a
b
c
d
e
f
5 nm
2 nm
1 nm
CoO (200)
CoO (200)

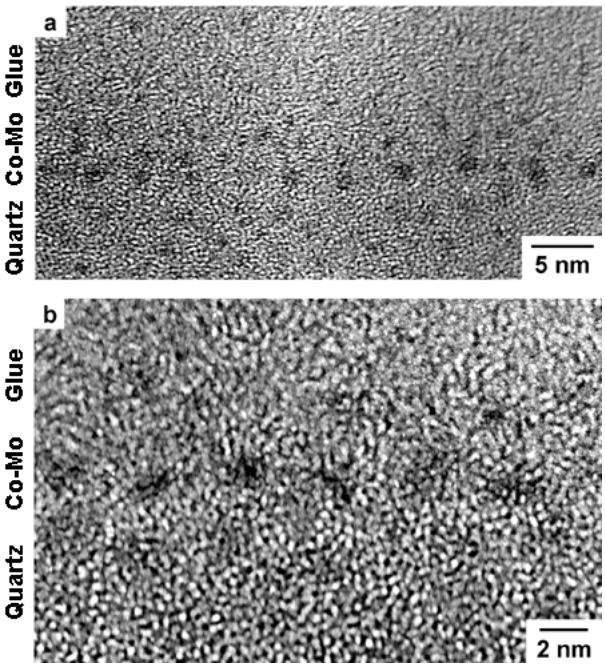
a
Quartz
Co-Mo
Glue
5 nm
b
Quartz
Co-Mo
Glue
2 nm

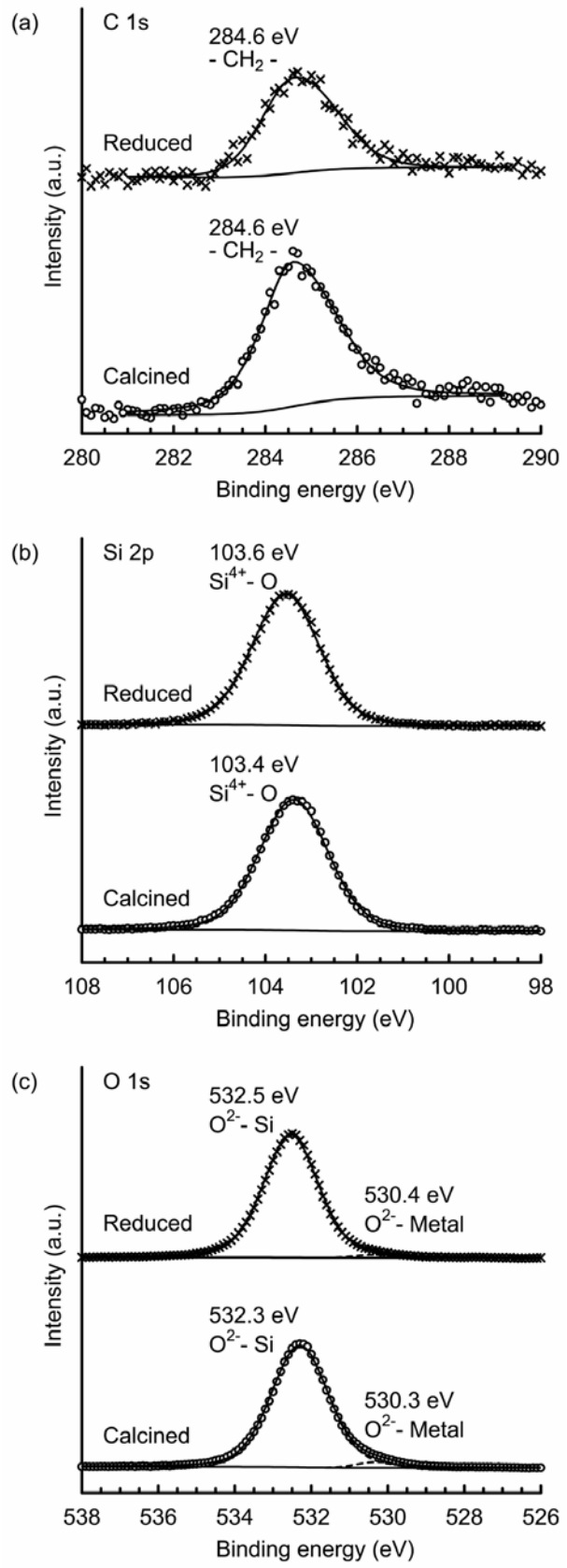
(a)
C 1s
284.6 eV
- CH2 -
Reduced
284.6 eV
- CH2 -
Calcined
Intensity (a.u.)
280
282
284
286
288
290
Binding energy (eV)
(b)
Si 2p
103.6 eV
Si4+ - O
Reduced
103.4 eV
Si4+ - O
Calcined
Intensity (a.u.)
108
106
104
102
100
98
Binding energy (eV)
(c)
O 1s
532.5 eV
O2- - Si
530.4 eV
O2- - Metal
Reduced
532.3 eV
O2- - Si
530.3 eV
O2- - Metal
Calcined
Intensity (a.u.)
538
536
534
532
530
528
526
Binding energy (eV)

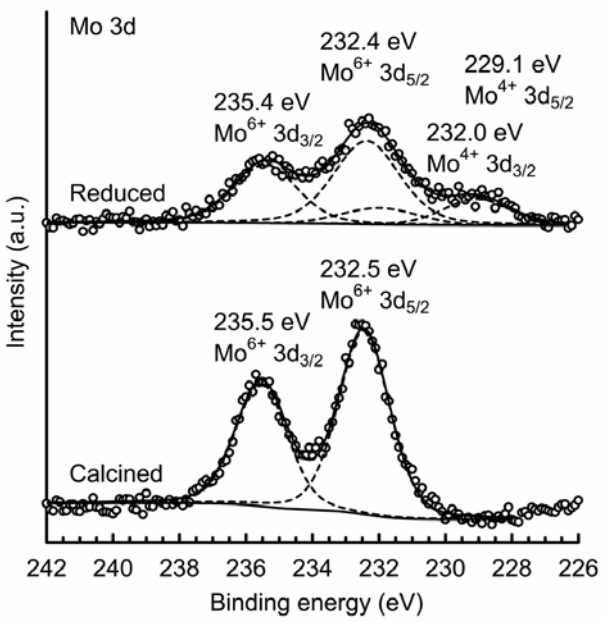
Mo 3d
232.4 eV
Mo6+ 3d5/2
229.1 eV
Mo4+ 3d5/2
235.4 eV
Mo6+ 3d3/2
232.0 eV
Mo4+ 3d3/2
Reduced
232.5 eV
Mo6+ 3d5/2
235.5 eV
Mo6+ 3d3/2
Calcined
Intensity (a.u.)
242 240 238 236 234 232 230 228 226
Binding energy (eV)

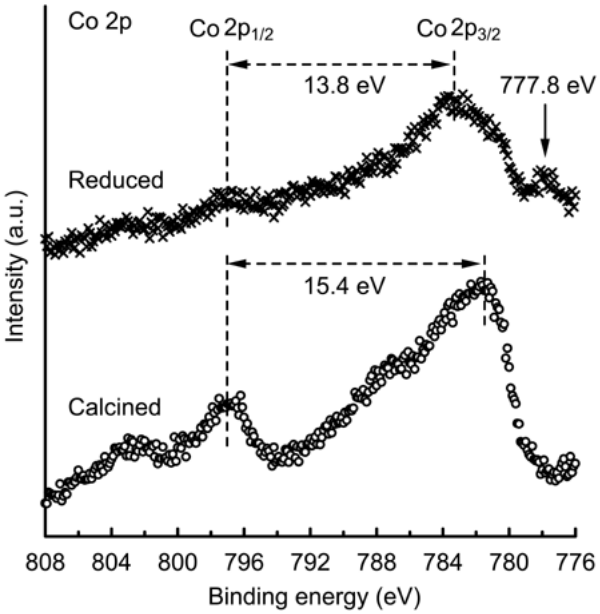
Co 2p
Co 2p1/2
Co 2p3/2
13.8 eV
777.8 eV
Reduced
15.4 eV
Calcined
Intensity (a.u.)
808
804
800
796
792
788
784
780
776
Binding energy (eV)

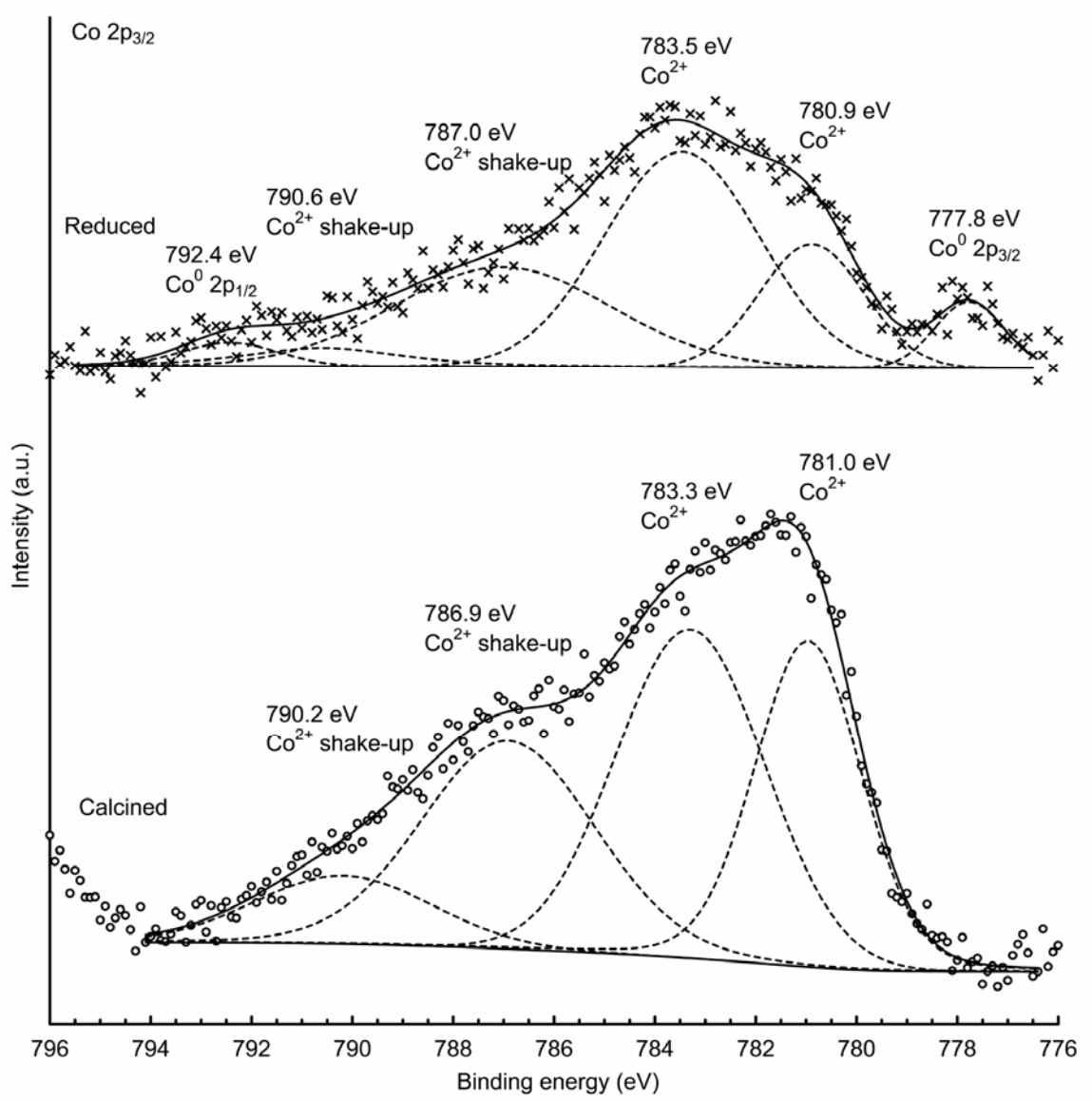
Co 2p3/2
783.5 eV
Co2+
780.9 eV
Co2+
787.0 eV
Co2+ shake-up
790.6 eV
Co2+ shake-up
Reduced
792.4 eV
Co0 2p1/2
777.8 eV
Co0 2p3/2
781.0 eV
Co2+
783.3 eV
Co2+
786.9 eV
Co2+ shake-up
790.2 eV
Co2+ shake-up
Calcined
Intensity (a.u.)
796
794
792
790
788
786
784
782
780
778
776
Binding energy (eV)

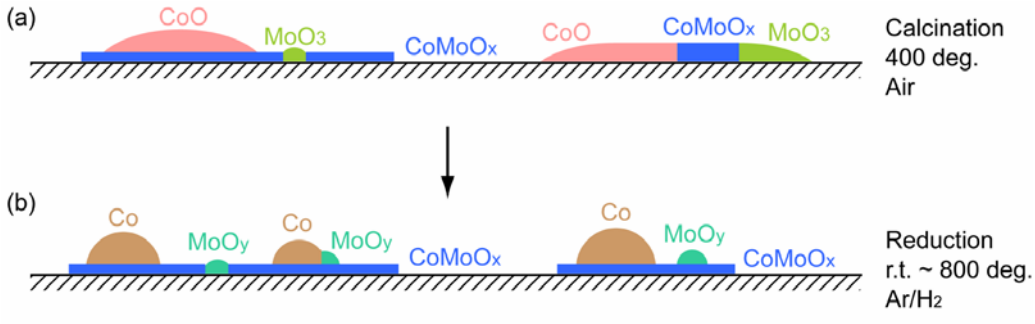
(a)
CoO
MoO3
CoMoOx
CoO
CoMoOx
MoO3
Calcination
400 deg.
Air
(b)
Co
MoOy
Co
MoOy
CoMoOx
Co
MoOy
CoMoOx
Reduction
r.t. ~ 800 deg.
Ar/H2